IOPscience iopscience.iop.org

Home Search Collections Journals About Contact us My IOPscience

MEMS-based thermally-actuated image stabilizer for cellular phone camera

This content has been downloaded from IOPscience. Please scroll down to see the full text.

2012 J. Micromech. Microeng. 22 115029

(http://iopscience.iop.org/0960-1317/22/11/115029)

View the table of contents for this issue, or go to the journal homepage for more

Download details:

IP Address: 140.113.38.11

This content was downloaded on 28/04/2014 at 09:35

Please note that terms and conditions apply.

J. Micromech. Microeng. **22** (2012) 115029 (12pp) doi:10.1088/0960-1317/22/11/115029

MEMS-based thermally-actuated image stabilizer for cellular phone camera

Chun-Ying Lin[1] **and Jin-Chern Chiou**[1,2]

[1] Department of Electrical and Control Engineering, National Chiao Tung University, Hsin-Chu, Taiwan, Republic of China
[2] School of Medicine, China Medical University, Taichung, Taiwan, Republic of China

E-mail: sikun.ece95g@nctu.edu.tw and chiou@mail.nctu.edu.tw

Received 28 June 2012, in final form 14 September 2012
Published 10 October 2012
Online at stacks.iop.org/JMM/22/115029

Abstract
This work develops an image stabilizer (IS) that is fabricated using micro-electro-mechanical system (MEMS) technology and is designed to counteract the vibrations when human using cellular phone cameras. The proposed IS has dimensions of $8.8 \times 8.8 \times 0.3$ mm^3 and is strong enough to suspend an image sensor. The processes that is utilized to fabricate the IS includes inductive coupled plasma (ICP) processes, reactive ion etching (RIE) processes and the flip-chip bonding method. The IS is designed to enable the electrical signals from the suspended image sensor to be successfully emitted out using signal output beams, and the maximum actuating distance of the stage exceeds 24.835 μm when the driving current is 155 mA. Depending on integration of MEMS device and designed controller, the proposed IS can decrease the hand tremor by 72.5%.

(Some figures may appear in colour only in the online journal)

1. Introduction

MEMS technology has the advantages of miniaturization and high precision and it is useful for fabricating micro *XY* stages [1]. Most methods for driving MEMS-based *XY* stages involve electrostatic actuators, which are utilized in most optical devices [2–7] and precise positioning systems [8] owing to high controllability and low power consumption. Applications of electrostatic devices include scanning probe microscopy [9, 10], data storage [11–13] and nano-position control applications [1, 14–16]. Except in electrostatic actuators, voice coil motors (VCM) are also used in most optical image stabilizer designs [17, 30]; however, since electrostatic actuators typically require a high driving voltage, the step-up circuit must be very large. VCMs require complex control strategies and they are larger especially thicker than MEMS-based devices. To overcome the disadvantages of electrostatic devices and VCMs and increase the output force, thermal actuators are designed to actuate the *XY* stage and perform an anti-shaking function [23]. Thermal actuators had been well developed in many applications, such as grating tuning by rhombic-shaped thermal actuator array [27], large displacement by SU8 thermal actuator [31], power efficiency increasing [32], fiber positioning assembly [33], a precisely position thermal actuator [34] and micro motors [35, 36].

The camera function is increasing more in cellular phones as well as meeting the consumer demand for increased pixels; image sensors of more pixels and DSLR functions are now being embedded in commercial cellular phones. Anti-shake technology is among the several new technologies that have been developed for mobile phones. Since increasing the number of camera pixels exacerbates the problem of image blurring that is caused by shaking of the human hand, an effective image stabilization method is required [17]. The most common image stabilization methods include lens shifting [18], image sensor shifting [19] and signal processing [20]. Signal processing, which is the anti-shaking technique that is used in most DSLRs, is now used in mobile phones. Although signal processing requires no additional hardware and does not influence the miniaturization of the system module, performance and reliability depend on the algorithm used, so the signal processing method typically requires large memory. Given the demand for the miniaturization of anti-shaking devices, lens shifting-based method exhibits less integration capability on a MEMS-based moving stage due to which currently only heavy and large commercial lens modules

 © 2012 IOP Publishing Ltd Printed in the UK & the USA

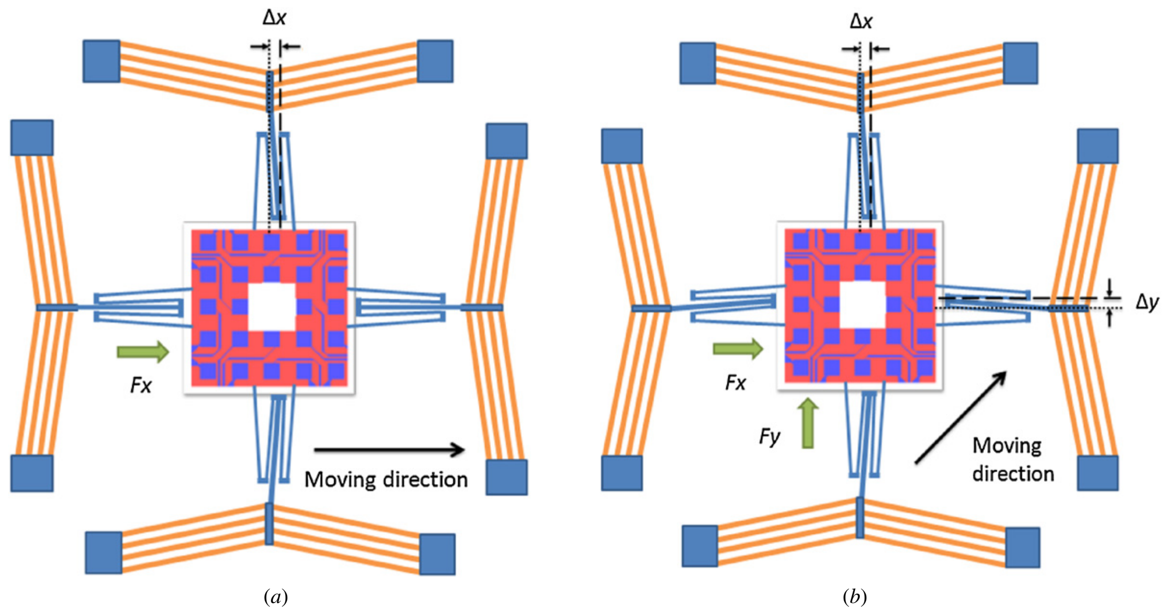

Figure 1. Driving modes of decoupled *XY* stage: (*a*) in the *x*-direction only and (*b*) in both *x*- and *y*-directions.

are available. Although image sensor shifting requires an actuating system, it is less affected by miniaturization, and the overall system is easier to miniaturize than in the lens shifting method [17]. The MEMS device supports a precise movement of suspended microstructures and the monolithic integration of microelectronic circuits on a chip [21]. Accordingly, an effective IS design is required to miniaturize cellular phone camera modules.

The MEMS-based decoupled thermal actuating *XY* stage that is developed in this work has several advantages, as follows. (1) Small chip size: since the presented *XY* stage is fabricated by the MEMS process, it is smaller than other anti-shaking devices. (2) Low driving voltage: the thermal actuating mechanism depends on a lower driving voltage and smaller step-up circuit than conventional actuators. (3) Simple control method: the image sensor shifting method directly compensates for blurred pixels, so complex control algorithms and optical path designs are unnecessary. Since the mass of the bare image chip is about 19 mg in this case, the small stage mass can be ignored. Also, the system stiffness in *x*-/*y*- and *z*-directions has to be larger than 187 and 190 to achieve stage sinking less than 1 μm in *z*-direction and resonant frequency higher than 500 Hz, respectively. The designed *XY* stage is suitable for a cellular phone that is equipped with a 3$\times$ zooming function, an actuator that can move at least 24.835 μm and a sufficiently strong structure to bear a 3.5 $\times$ 3.5 $\times$ 0.1 mm^3 IS load, from which it must be decoupled in two dimensions when driven. Therefore, the proposed design has a high aspect ratio and 100 μm thick silicon springs. Four decoupling springs are connected to the main suspended structures and the shuttle for lateral displacement isolation. The process for fabricating the *XY* stage involves double-side lithography, two ICP etching processes and the flip-chip bonding process. The electrical connection of the output is routed and carries 24 outputs. The required displacement of anti-shaking function is achieved when the *XY* stage is driven in a direction of motion, and the decoupled effect in the perpendicular direction is excellent by the flexure beam designs.

2. Concept and structure design

The proposed MEMS-based image stabilizer is an *XY* stage that can carry an image sensor and compensate for blurring that is caused by shaking. The *XY* stage structure involves decoupling beams, thermal actuators, piezoresistive displacement sensors (PRDS) and SU8 isolators.

2.1. Design of XY stage

The IS that is developed herein is designed to minimize the size of the device that is used to suspend an image sensor and to provide excellent decoupled performance. The decoupling beams of an *XY* stage are connected to thermal actuators and perform an anti-shaking function that compensates for the shaking of the human hand, without causing parasitic motion in other directions. Figure 1(*a*) schematically depicts the *XY* stage. When a single direction force F_x is supplied to the decoupled structure, it is displaced Δx in the *x*-direction, and the parasitic displacement in the *y*-direction is negligible. Figure 1(*b*) presents a simplified operating mechanism of the proposed decoupled *XY* stage when different forces are applied in the *x*- and *y*-directions. The decoupled design assumes ideal displacement without parasitic errors in the *x*- and *y*-directions (Δx and Δy, respectively) and ideal mechanical isolation between the two orthogonal driving directions.

To provide excellent stiffness of the device that suspends the image sensor without deflection in the *z*-direction, the 100 μm thick *XY* stage is designed and fabricated in this work. Flip-chip bonding, wire bonding, routing springs and electrode pads are utilized to form electrical connections among the image sensor, device structure and the output of the PCB pads.

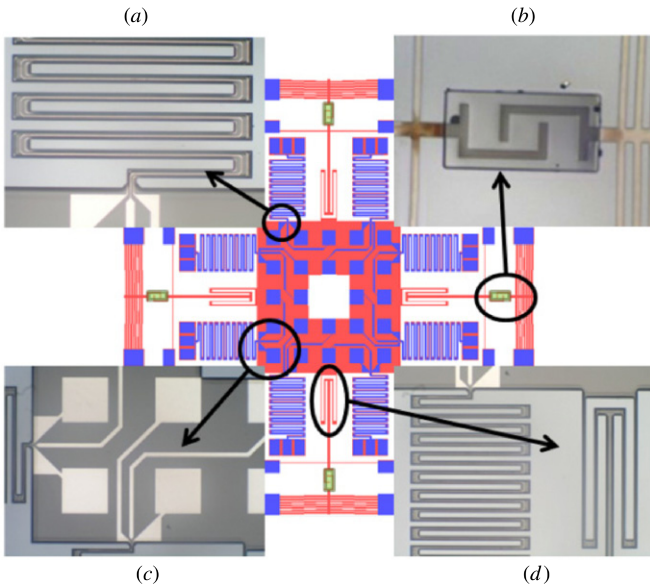

Figure 2. Structure of the *XY* stage. (*a*) Signal output beam. (*b*) PRDS, SU8 isolator and thermal actuator. (*c*) Electrode pads. (*d*) Decoupling beam.

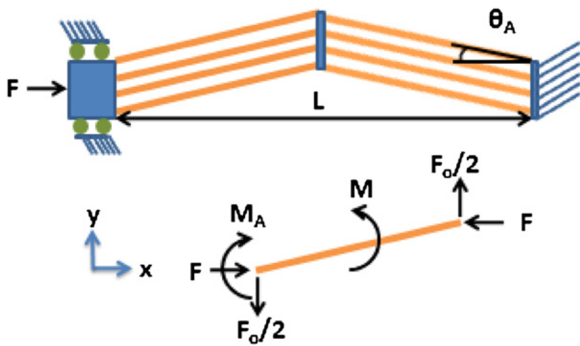

Figure 3. Force on chevron thermal actuator.

Figure 2 schematically depicts the complete device; separated decoupling used in each direction satisfies the kinematical design requirements. Each thermally driven actuator has a push-only design, and each operates in only one direction -*X*+, *X*–, *Y*+, or *Y*–. This work focuses on the pitch- and yaw-axis tremor compensation by equivalent displacements in *x*- and *y*-directions. However, rotations in roll-axis and angular displacement in the θ_Z direction are not compensated herein.

The springs of the *XY* stage are arranged symmetrically, and the electrical routings are arranged in a balanced layout with two signal output springs in each direction. The signal output springs are designed to be as thin as possible to minimize their effect on the overall spring constant of the system. The isolation layers and the isolator SU8 ensure that the electric signals between each structure and the signal output are mutually independent.

2.2. Operating principles of electro-thermal chevron actuator

An electro-thermal mechanical force drives the developed *XY* stage. Figure 3 schematically depicts the electro-thermal chevron actuator. An electro-thermal mechanical force that

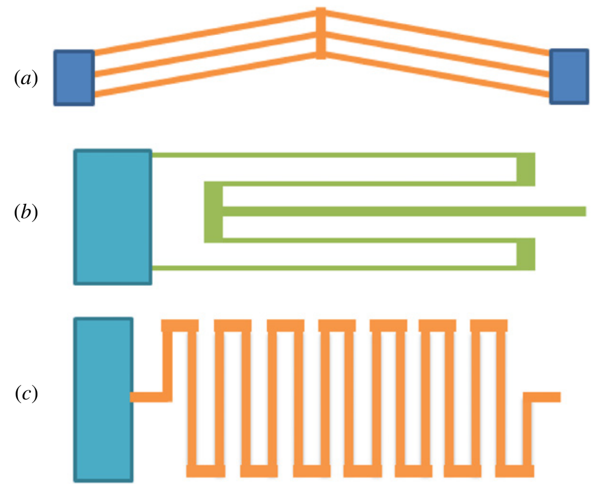

Figure 4. (*a*) Thermal actuator beams. (*b*) Decoupling beams. (*c*) Folded flexure beams.

is generated by supplying a current changes the relative displacement between the *XY* stage and the pads.

In estimating the driving displacement, several boundary conditions and assumptions are applied: (1) the actuator is heated uniformly; (2) the pads is at a fixed temperature of 300 K, and (3) the expansion coefficient is a constant and equals the Si expansion coefficient, 3.7 ppm K^{-1} and Si thermal conductivity 85 W m^{-1} K. Under these conditions, the driving displacement is a linear function of temperature. The equation and boundary conditions for predicting driving displacement are as follows [24]:

$$EI\frac{\partial^2 y}{\partial^2 x} = M = M_A - Fy - F_o x/2 \tag{1}$$

$$y|_{x=0} = 0;\ \left.\frac{\delta y}{\delta x}\right|_{x=0} = \left.\frac{\delta y}{\delta x}\right|_{x=L/2} = \tan\theta_A;$$

$$\sigma = \Delta T E\alpha = \frac{E}{L}\left(\Delta L + \frac{FL}{EWT}\right), \tag{2}$$

where *EI* is the flexural rigidity; *F* is the reaction force in the *x*-direction that is used to model the effects of thermal stress and F_o is the output force. The terms *L*, *W* and *T* in figure 3 denote the length, width and thickness of the actuator, respectively. The term ΔT is the change in temperature; ΔL denotes the change in *L* due to *F* and α is the thermal expansion coefficient. Peak deflection is obtained by setting the output force to zero, and peak output force is obtained by setting the deflection to zero. The equation yields the relationship between the lateral force for the peak deflection and peak output force is shown in (3). This equation also yields the peak output force; therefore, the output forces and displacements of thermal actuators in different dimensions can be calculated by

$$F_{o\max} = 2F_{\max}\tan\theta_A. \tag{3}$$

2.3. Designing and estimating spring stiffness

Figure 4 presents the three flexure beams that are used herein. Figure 4(*a*) is a chevron thermal actuator. The small pre-bending angle allows the actuator model to be simplified as

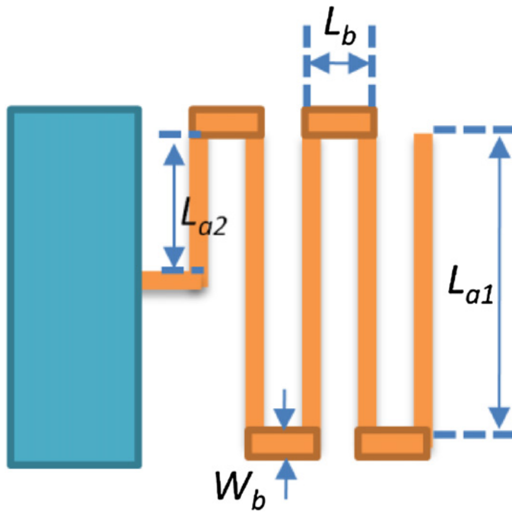

Figure 5. Model of folded-flexure spring.

Table 1. Flexure beam specifications.

Spring type	Figure 4(*a*)	Figure 4(*b*)	Figure 4(*c*)
Length	*La1*:630 μm *La2*:300 μm	*L*:2000 μm	*La1*:900 μm *La2*:790 μm
Width	30 μm	20 μm	25 μm
Height	100 μm	100 μm	100 μm

parallel clamped–clamped beams [10]. Figure 4(*b*) presents the decoupling beam. According to the past research [25], the decouple ratio must be larger than 10 when the pixels are smaller than 2.5 μm. Figure 4(*c*) presents the signal output beam and figure 5 presents the folded-flexure beam in the structure [11]. Table 1 presents the flexure beam specifications in this work.

2.4. Motion range analysis of decoupled XY stage

Most commercial cellular phones have built-in multi-megapixel cameras but lack an optical anti-shaking function. Since shaking is difficult to avoid when using a cellular phone camera, blurring is common. Figure 6 plots the relationship between the number of blurred pixels and the angle of hand shaking. When the camera moves through an angle $d\theta$ in the horizontal plane, the number of blurred pixels is

$$BP = \frac{d\theta}{\theta_L} P_H, \tag{4}$$

where θ_L is the horizontal angle and P_H is the total number of pixels along the horizontal. According to experimental data [22] and calculations [25, 26], compensation for a camera with a 3 × zoom function requires an actuating displacement of the *XY* stage that exceeds 24.42 μm.

3. System modeling and FEA simulation

The decoupled effect, stiffness and natural frequency of the designed image stabilizer are elucidated in a simulated actuator that is developed using the IntelliSuite finite elements analysis (FEA) software. The software is used for static simulation of the in-plane distance moved by the IS and its coupled mechanical interference in each orthogonal direction. Figure 7 presents the simulation results that are related to the decoupling effect. Notably, non-decoupled related structures are excluded. The simulation is based on the following actual boundary conditions. (1) The anchor is neglected because it is attached to the substrate and does not influence the results of the simulation. (2) The shuttle and flexure beams are suspended and free in air. A significant decoupling effect in the *x*- and *y*-directions can thus be simulated (figures 7(*a*) and (*b*)). In the simulation, a force F_y causes a 31 μm displacement in the *y*-direction and only a 0.32 μm displacement in the *x*-direction. The simulation verifies the excellent decoupling in the design of the movable springs, which clearly satisfies the decoupled requirement. Although the force output can be increased by adding thermal actuators in series, the use of more actuators in series consumes more power. Therefore, as a trade-off between the output force and the driving current, the number of proposed thermal actuators in series is set to three.

To determine the resonant frequency and shapes of the designed structure, Intellisuite FEM software is also performed to verify the vibration characteristics. The following equation shows the resonant frequency:

$$F_{\text{resonant}} = \frac{1}{2\pi}\sqrt{\frac{k}{M}} \tag{5}$$

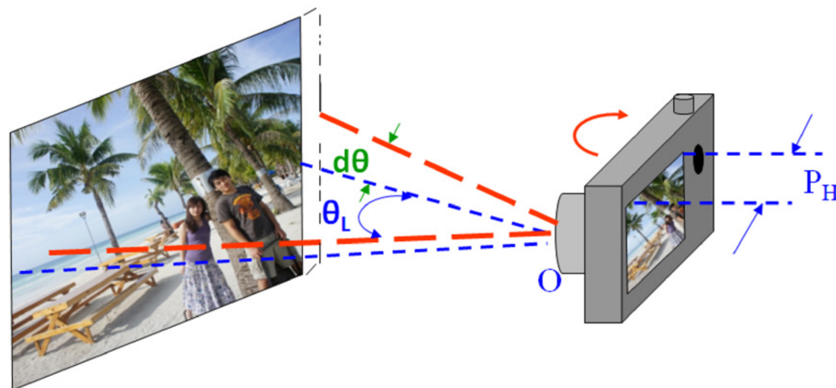

Figure 6. Relationship of blurred pixels and hand-shaking angle.

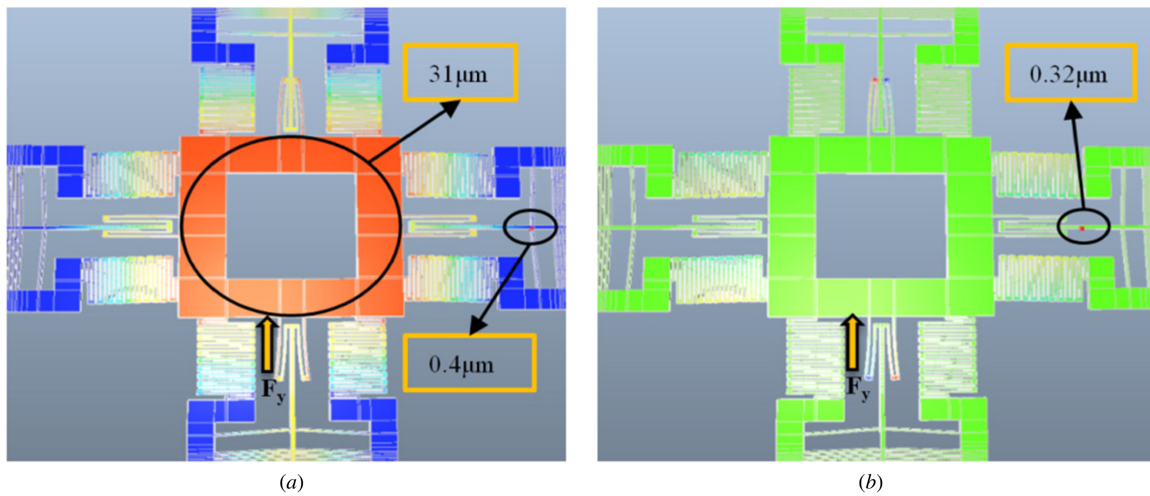

(*a*) (*b*)

Figure 7. Displacement in (*a*) *y*-direction and (*b*) *x*-direction when force is exerted in the *y*-direction.

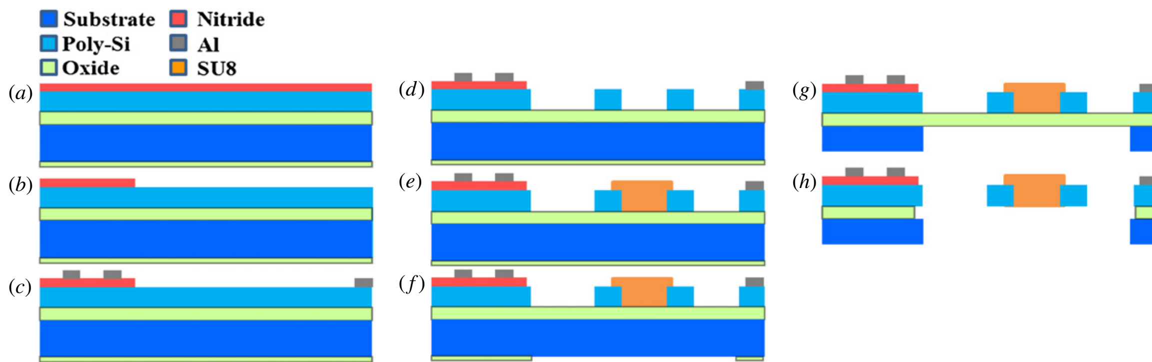

Figure 8. Fabrication of *XY* stage: (*a*) deposition of bottom oxide and nitride (oxide: 1 μm, nitride: 0.5 μm), (*b*) patterning of nitride, (*c*) patterning of Al (1 μm), (*d*) patterning of device layer, (*e*) patterning of SU8, (*f*) patterning of bottom oxide, (*g*) patterning of bottom layer (350 μm) and (*h*) release.

where k is the system stiffness of IS, M is the overall mass, and F_{resonant} is the resonant frequency of the *XY* stage. Because the structure is symmetrical, the simulated resonant frequency is 8175 Hz with movement in *x*- and *y*-direction.

4. Fabrication

4.1. Fabrication processes

The fabrication of developed IS includes various processes. These are device layer formation, substrate formation, and the final combination of image sensor and shuttle. Figure 8 shows the processes for fabricating the device layer and the substrate; the steps are structure definition, patterning of the isolator SU8, circuit routing and patterning of the bottom layer. The fabrication begins with a (1 0 0) SOI wafer. The thickness of the device layer, oxide layer and substrate are 100, 1 and 350 μm, respectively.

The fabrication process comprises the following steps.

(a) Following basic RCA cleaning, the CVD process is utilized and a 0.5 μm thick nitride layer on the top and a 2 μm thick silicon oxide layer on the bottom of the SOI wafer is deposited.
(b) During photolithography, the nitride is patterned to form the electric isolation layer between the shuttle and the circuit on the top of the SOI wafer.
(c) A 1 μm thick Al layer is deposited by dc sputtering and patterned to form the circuits and pads. The device structure is patterned using the first ICP process to a depth of 100 μm.
(d) SU8 is patterned to isolate the heat and electricity in the actuators from the shuttle. The RIE process is utilized to pattern the bottom oxide layer to form a hard mask.
(e) The second ICP process is utilized to define the suspending area on the back of the SOI wafer.
(f) The structure is released by the RIE process.

Figure 9 presents scanning electron microscopic (SEM) images following the deformation of the device.

4.2. Flip-chip bonding

Figure 10 presents an image sensor that is combined with the *XY* stage using the flip-chip method. Figure 11 shows the packaging process captured from the flip-chip bonder monitor. Figures 11(*a*)–(*c*) present the process by which image sensor is absorbed by pick-up head. Before absorption, the spectroscope

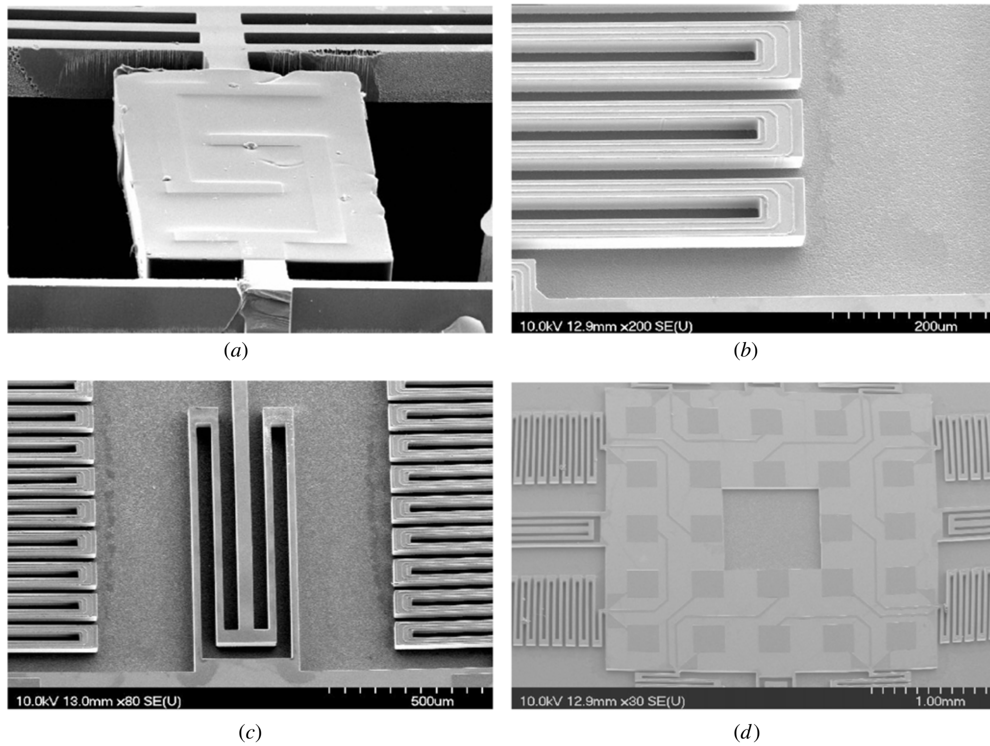

Figure 9. SEM images of *XY* stage: (*a*) SU8 isolator, (*b*) micro electrical wires, (*c*) decoupling beam and (*d*) shuttle.

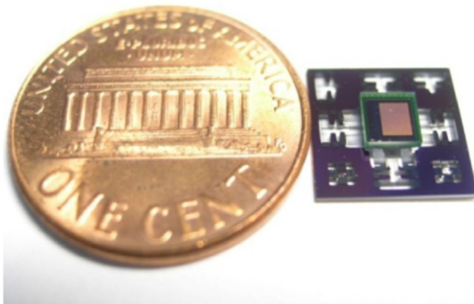

Figure 10. *XY* stage following flip-chip bonding.

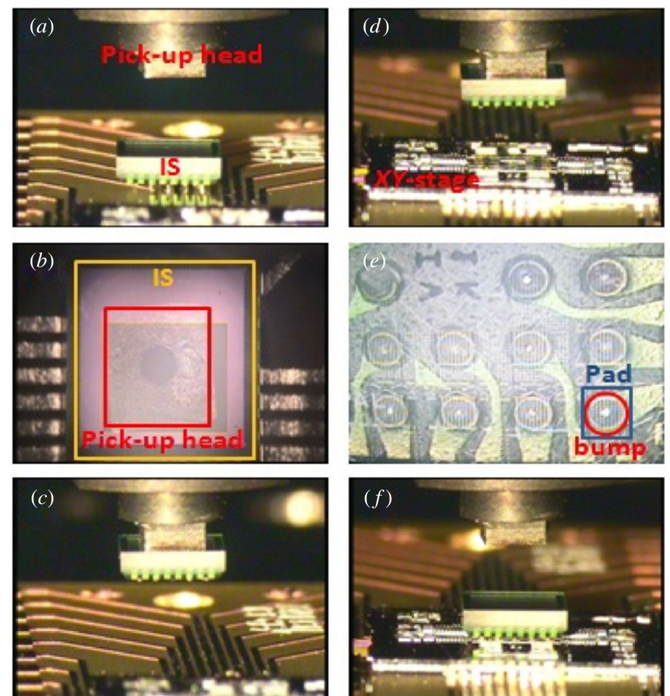

Figure 11. Flip-chip bonding process.

is used to align the pick-up head with the sensor (figure 11(*b*)). Figures 11(*d*)–(*f*) show how the sensor bumps are aligned with the shuttle pads. After alignment, a force of 2N is applied and the bumps are reflowed to 235 °C; then, the pick-up head releases the image sensor to complete the bonding process, as presented in figures 11(*e*) and (*f*).

5. Experimental results

Experiments that were carried out to evaluate the effectiveness of the proposed IS included the measurement of actuating displacement and resonant frequency using a MEMS motion analyzer (MMA). When the *XY* stage was driven to 24.835 μm in the *y*-direction, the displacement in the *x*-direction was only 1.3 μm (figure 12). The experimental decoupling ratio in the two directions was 19.1, which exceeded the minimum ratio of ten that is required by the system. Figure 13 plots the dynamic measurements: the resonant frequency of the *XY* stage is 8000 Hz, falling to 1460 Hz after attachment of the accelerometer (figure 21). Figure 14 presents the thermal imaging results. The red and blue triangles represent the maximum and minimum temperatures of the actuator when current output of 155 mA was applied to the actuator. The figure reveals that the temperature is highest in the middle of the actuator and that the pads are close to room temperature. Furthermore, a comparison of figures 14(*a*) and (*b*) reveals

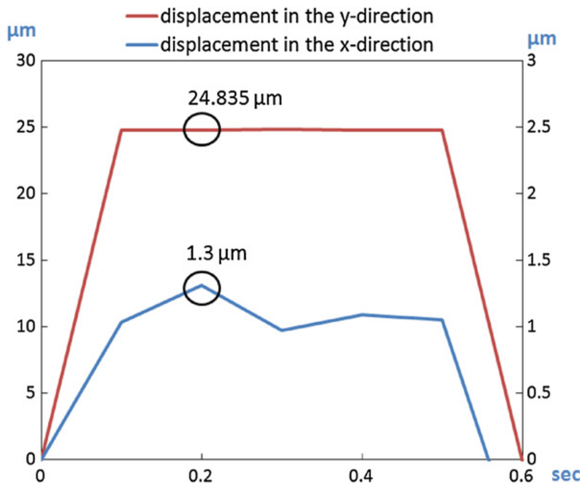

Figure 12. Displacement in *x*- and *y*-directions.

that the maximum temperature of the thermal actuator is 353 °C without an SU8 isolator and 408 °C with a SU8 isolator. Accordingly, the isolator design enables a lower driving current to achieve the same actuating displacement. In general, the actuating displacement of the *XY* stage and operating temperature are 9–20 μm, 250–550 °C or 0–9 μm, less than 250 °C with/without the zooming condition.

6. Control implementation

The controllable actuator and the feedback mechanism must be established before a control method can be implemented. In the actuating part of the IS system, the linear actuator will increase the controllability of *XY* stage, and the supply of a suitable controllable power source is important. In the sensing part of the IS system, a properly designed filter can reduce the effect of noise and increase the accuracy of the controller. In this work, power supply, filters, amplifiers and the controller are implemented using commercial chips and the software LabVIEW.

6.1. Actuating circuit

To control the current precisely, operational amplifier and Darlington transistor pairs are used to generate the current (figure 15(*a*)), where R_s is a tunable resistance that can be set to satisfy requirements of the system, and relationship between

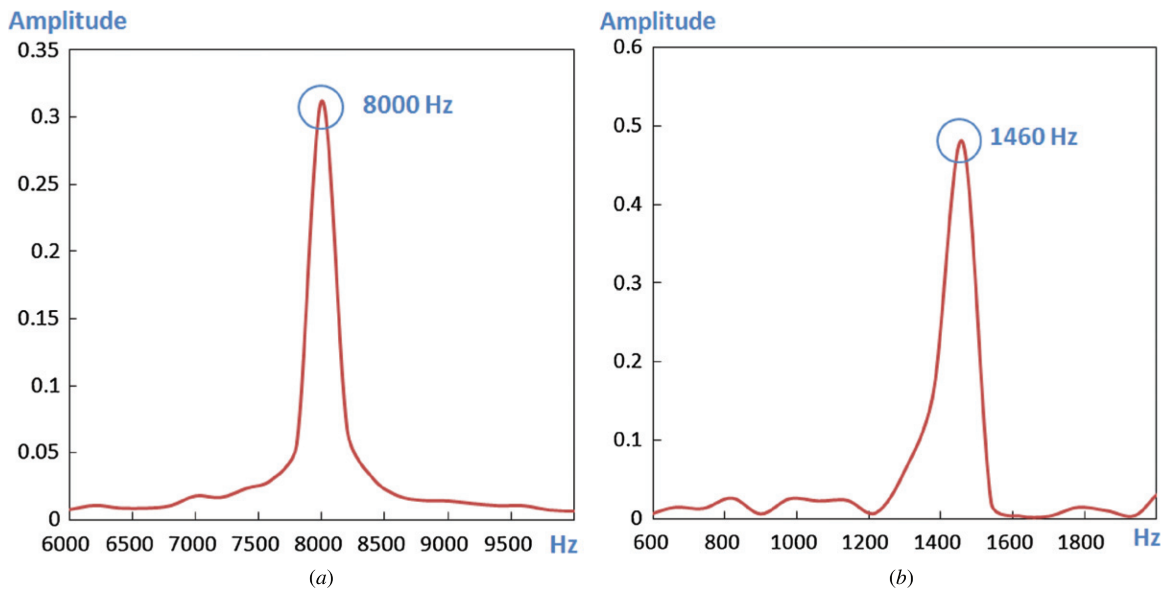

(*a*) (*b*)

Figure 13. Resonant frequency of *XY* stage (*a*) without attached chip, (*b*) with attached chip.

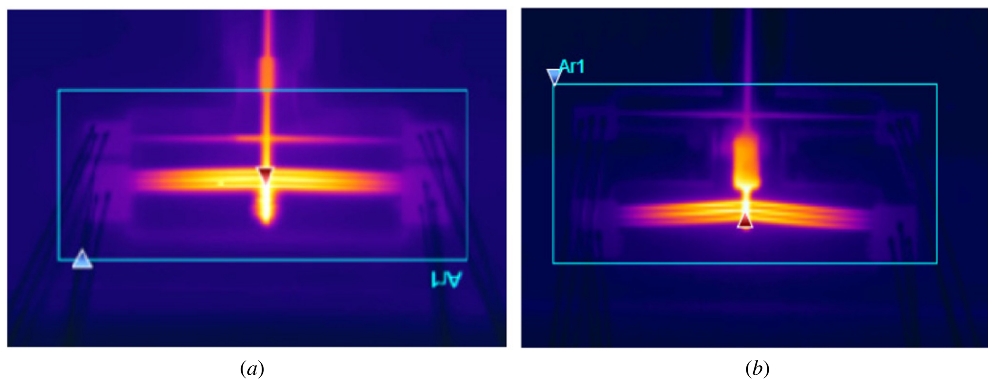

(*a*) (*b*)

Figure 14. Thermal imaging measurements. (*a*) Thermal actuator without isolator. (*b*) Thermal actuator with isolator.

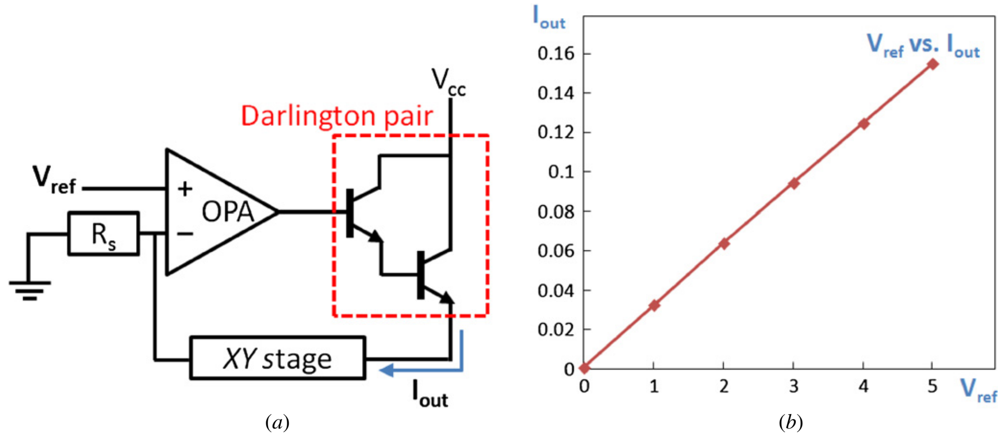

(*a*) (*b*)

Figure 15. (*a*) Actuating circuit, and (*b*) reference voltage versus current output.

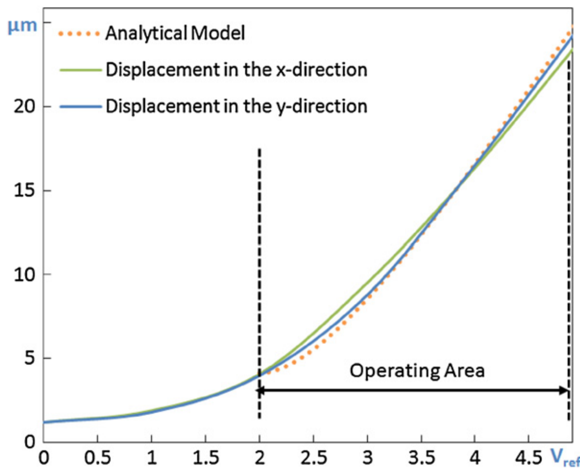

Figure 16. V_{ref} versus displacement, as measured by MMA.

reference voltage and current output is measured as presented in figure 15(*b*).

This simple actuating circuit can be used to control the current output in the range 0 to 155 mA. The maximum displacement of the *XY* stage is about 24.835 μm in the operating area. Figure 16 presents the *XY* stage displacements in *x*- and *y*-directions measured by MMA when V_{ref} was varied from 0 to 5 V. To increase linearity, the operating area was set in the range of 2–5 V.

6.2. Sensing circuit

A PRDS is used to feedback a displacement signal to the controller of the *XY* stage system. Figure 17 presents the Wheatstone bridge sensing circuit, where R_{ref} and R_{sensor} are reference resistance and PRDS resistance, and R_{tunable} is the tunable resistance, which can be varied according to the PRDS resistance. To reduce noise, the batteries are used to supply power to the sensing circuit. Following equation yields V_{sense} when $R_{\mathrm{sensor}} = R_{\mathrm{tunable}} + \Delta R_{\mathrm{sensor}}$:

$$\Delta V_{\mathrm{sense}} = V_{\mathrm{battery}} \times \left[\frac{R_{\mathrm{tunable}} + \Delta R_{\mathrm{sensor}}}{R_{\mathrm{ref}} + R_{\mathrm{tunable}} + \Delta R_{\mathrm{sensor}}} - \frac{R_{\mathrm{tunable}}}{R_{\mathrm{ref}} + R_{\mathrm{tunable}}}\right]. \quad (6)$$

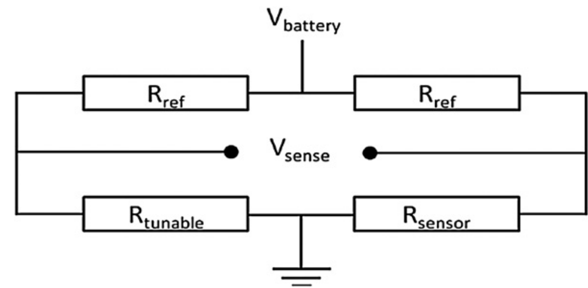

Figure 17. Sensing circuit.

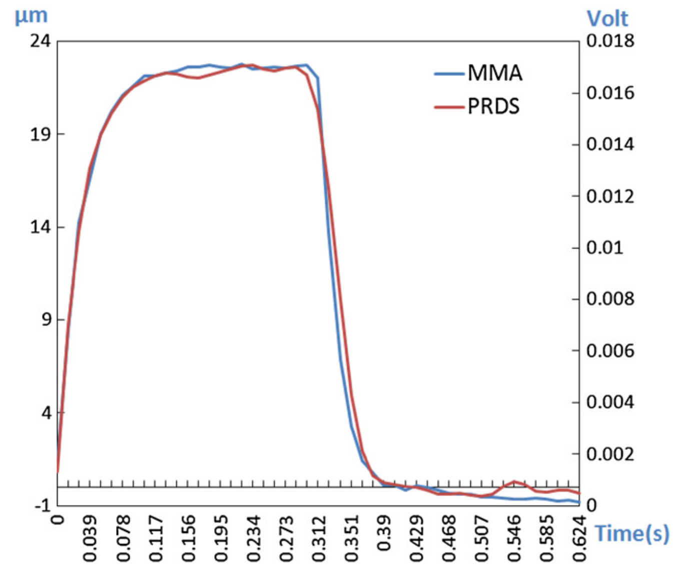

Figure 18. Comparison of measurements obtained using the MMA and PRDS.

Since $\Delta R_{\mathrm{sensor}}$ is much less than the sum of R_{ref} and R_{tunable} (6) can be modified to (7), and the sensitivity given by (8)

$$\Delta V_{\mathrm{sense}} = V_{\mathrm{battery}} \times \left[\frac{\Delta R_{\mathrm{sensor}}}{R_{\mathrm{ref}} + R_{\mathrm{tunable}}}\right] \quad (7)$$

$$\text{sensitivity} = V_{\mathrm{battery}} \times \left[\frac{\Delta V_{\mathrm{sense}}}{\text{displacement}}\right]. \quad (8)$$

To confirm the feasibility of using the PRDS, measurements obtained using the MMA and PRDS are compared, as presented in figure 18. The experimental results are very

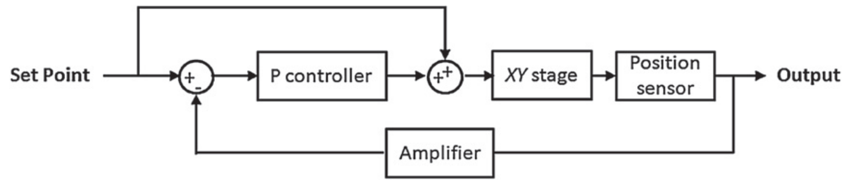

Figure 19. Block diagram of modified proportional controller.

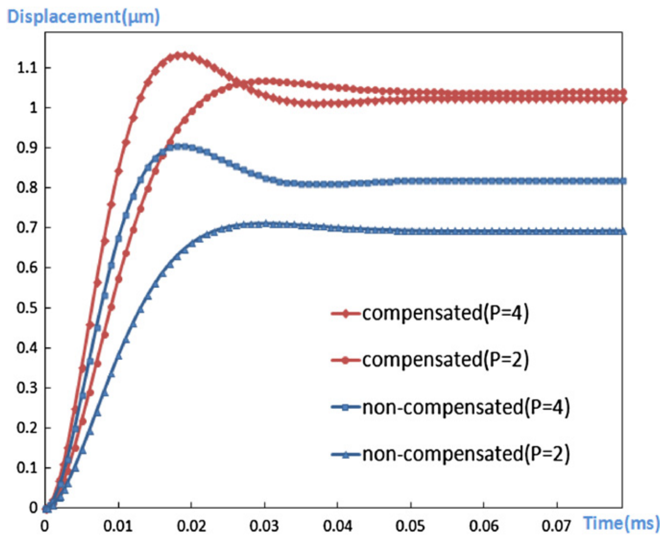

Figure 20. Comparison of compensated and non-compensated proportional controller.

close: the correlation between the two sets of measurements is 99.774%, and the sensitivity is approximately 0.77 mV μm^{-1}.

6.3. Controller design

The PID controller is a popular control mechanism that is used in many industrial control systems. It calculates an error as the difference between a measured process variable and a desired set point. However, high-frequency noise that occurs in a PRDS will be amplified by the derivative part of PID controller [34]. To avoid this situation, only the proportional part of PID controller is applied herein because it is simple and improves the response time of the system without amplifying the high-frequency noise. To compensate for the steady-state error of the proportional controller, a proportional controller with compensated loop is used to control the *XY* stage (figure 19). Results of compensated and non-compensated controllers are simulated by math software SimuLink and the steady-state error is eliminated after compensation, as shown in figure 20.

To determine the suitable proportional parameter, various step wave tests with different proportional parameters are tuned and measured using a PRDS, as presented in figure 21(*a*). A larger proportional parameter yields a smaller rise time, but causes a larger overshoot. To avoid overshooting more than 10%, the proportional parameter is set to four herein. Under this condition, the rising time decreases from 41 to 13 ms and the overshooting is 9.53%, as presented in figure 21(*b*). Besides, according to simulation results in figure 22, the bandwidth can be improved from 6 to 35.77 Hz by using the designed controller.

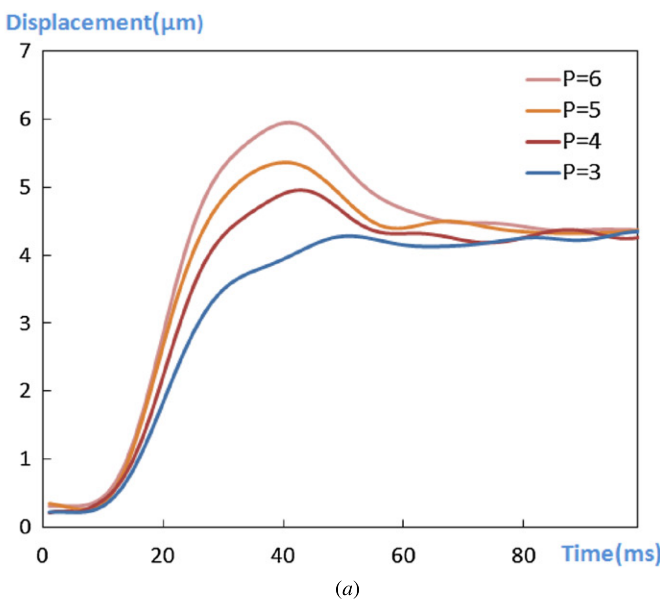

(*a*)

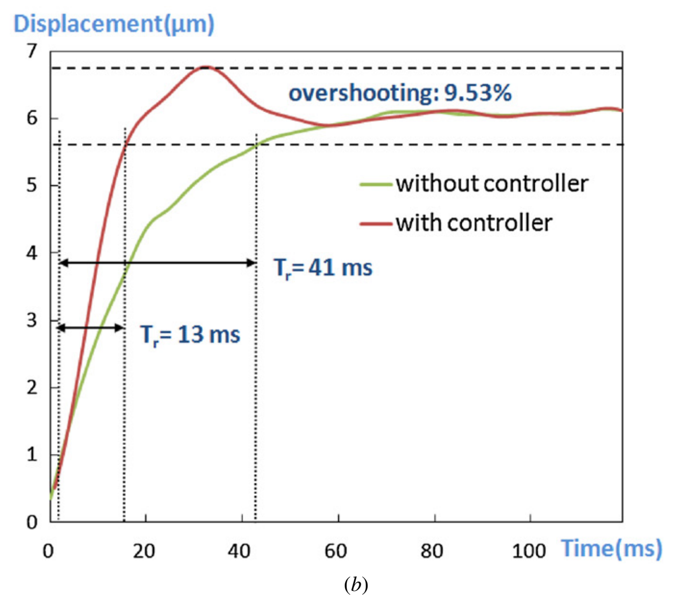

(*b*)

Figure 21. Results of (*a*) step wave test, (*b*) rising time and overshooting.

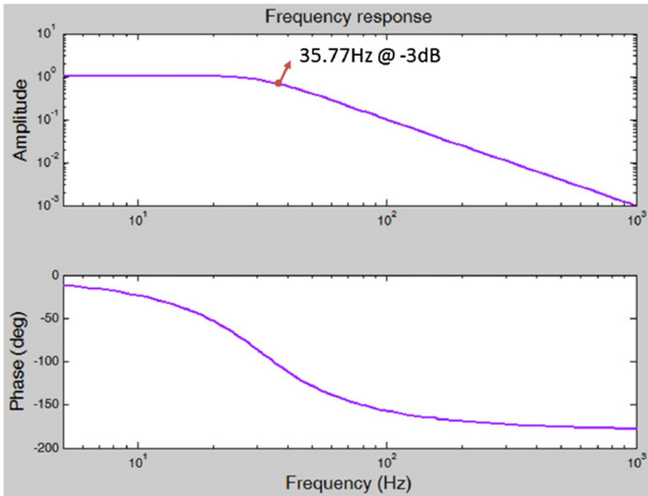

Figure 22. Frequency response of the IS.

6.4. *Compensation for hand tremor*

To measure hand tremor and confirm the functionality of IS, a commercial accelerometer (ADXL322) is attached to the shuttle using a flip-chip bonder and a wire bonder, as presented in figure 23.

The commonly frequency of hand tremor is in range of 5–15 Hz and the amplitude is approximately 15 *mg*, where *g* is gravitational acceleration [28, 29, 37]. To confirm the efficiency of the IS, an artificial tremor was applied and the acceleration intensity was measured by the attached accelerometer to be 19.9 *mg*. Compensation by the proposed IS and designed controller reduced the rms acceleration to 5.5 *mg*, as presented in figure 24, where blue line is the hand tremor signal and red line is voltage output of controller. Generally, cameras require a shuttle speed of the reciprocal of focal length second or faster to prevent image blurring, the proposed IS decreases the hand tremor by 72.5%; therefore, the equivalent effect of a shutter speed is approximately 1.9 stops faster.

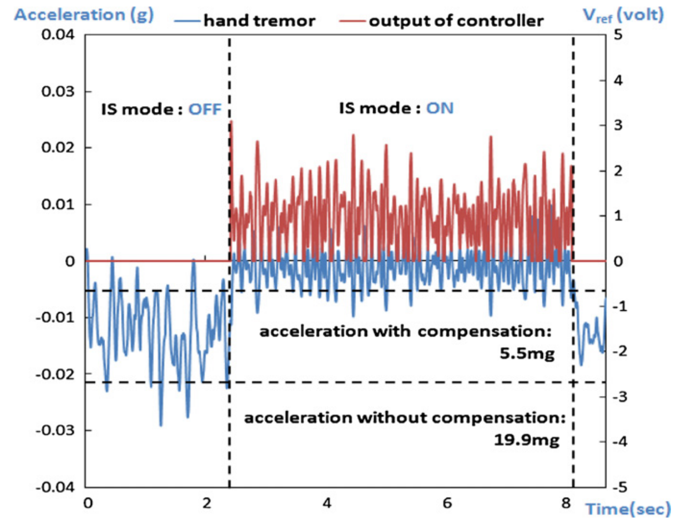

Figure 24. Results of efficiency test of proposed IS.

7. Conclusion

In this work, a micro decoupled *XY* stage was simulated, fabricated, tested and integrated with a designed controller for image stabilization. The *XY* stage was designed to load an image sensor, which was accurately attached to the shuttle by flip-chip bonding. The image sensor was connected to the output circuits using signal output beams. The proposed IS has the potential to be used in commercial cellular phone cameras because of its anti-shaking function. Experimental results reveal that a driving current of 155 mA causes a 24.835 μm displacement in the driving direction and only a 1.3 μm displacement in the vertical direction. These values suffice for effective anti-shaking. The results in the *x*- and *y*-direction are similar because the design is symmetrical. The isolator SU8 not only insulates the heat flux and driving current, but also increases the actuating displacement for the same driving currents. The natural frequency of the proposed *XY* stage design is approximately 8000 Hz and falling to 1460 Hz after the attachment of accelerometer, the rising time is approximately 41 ms and decreased to 13 ms by using the designed controller. After the integration of the device, the

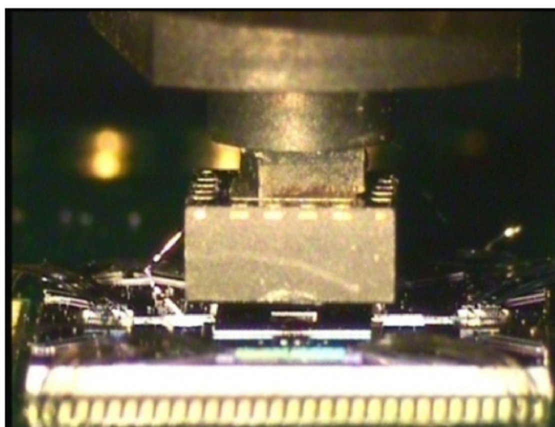

(*a*)

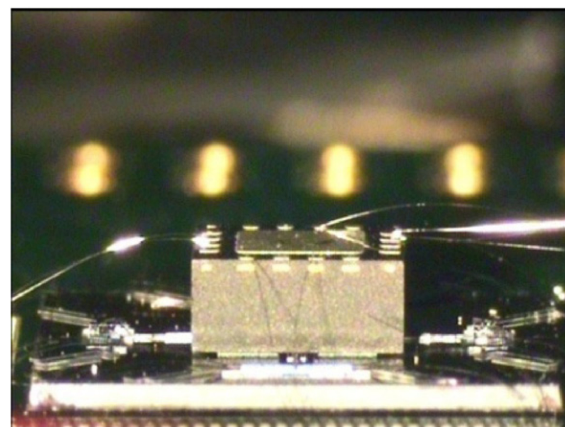

(*b*)

Figure 23. Attachment of accelerometer in (*a*) flip-chin bonding, (*b*) wire bonding.

proposed IS can decrease the hand tremor by 72.5% and give equivalent effect of a shutter speed 1.9 stops faster.

Acknowledgments

This work was supported in part by National Science Council, Taiwan, under Contract 100-2220-E-009-032, 100-2220-E-009-019, and in part by Taiwan Department of Health Clinical Trial and Research Center of Excellence under contract nos DOH99-TD-B-111-004 and DOH99-TD-C-111-005. This work was also supported in part by the UST-UCSD International Center of Excellence in Advanced Bio-engineering sponsored by the Taiwan National Science Council I-RiCE Program under grant no. NSC-100-2911-I-009-101. This paper is particularly supported by 'Aim for the Top University Plan' of the National Chiao Tung University and Ministry of Education, Taiwan, R.O.C. Ted Knoy is appreciated for his editorial assistance.

References

[1] Sun Lining, Wang Jiachou, Rong Weibin, Li Xinxin and Bao Haifei 2008 A silicon integrated micro nano-positioning *XY*-stage for nano-manipulation *J. Micromech. Microeng.* **18** 125004

[2] Takahashi K, Mita M, Fujita H and Toshiyoshi H 2006 A high fill-factor comb-driven *XY*-stage with topological layer switch architecture *IEICE Electron. Express* **3** 197–202

[3] Kwon H N, Lee J-H, Takahashi K and Toshiyoshi H 2006 Micro *XY* stages with spider-leg actuators for two-dimensional optical scanning *Sensors Actuators* A **130–131** 468–77

[4] Kwon S and Lee L P 2002 Stacked two dimensional micro-lens scanner for micro confocal imaging array *Proc. IEEE Int. Conf. on Micro Electro Mechanical Systems* pp 483–6

[5] Laszczyk K, Bargiel S, Gorecki C and Krezel J 2008 Towards integration of glass microlens with silicon comb-drive *X–Y* microstage *IEEE/LEOS Int. Conf. on Optical MEMS and Nanophotonics* pp 168–9

[6] Yasumura K Y, Grade J D and Jerman H 2002 Fluid damping of an electrostatic actuator for optical switching applications *Proc. Solid-State Sensor, Actuator and Microsystems Workshop* pp 358–61

[7] Takahashi K, Kwon H N, Mita M, Saruta K, Lee J-H, Fujita H and Toshiyoshi H 2007 A silicon micromachined f-θ microlens scanner array by double-deck device design technique *IEEE J. Sel. Top. Quantum Electron.* **13** 277–82

[8] Yang J P, Mou J Q, Chong N B, Lu Y, Zhu H, Jiang Q, Kim W G, Chen J, Guo G X and Ong E H 2007 Probe recording technology using novel MEMS devices *Microsyst. Technol.* **13** 733–40

[9] Ando Y 2004 Development of three-dimensional electrostatic stages for scanning probe microscope *Sensors Actuators* A **114** 285–91

[10] Indermuhle P F, Linder C, Brugger J, Jaecklin V P and de Rooij N F 1994 Design and fabrication of an overhanging *XY*-microactuator with integrated tip for scanning surface profiling *Sensors Actuators* **43** 346–50

[11] Kawai Y, Ono T, Esashi M, Meyer E and Gerber C 2007 Resonator combined with a piezoelectric actuator for chemical analysis by force microscopy *Rev. Sci. Instrum.* **78** 063709

[12] Kim C H, Jeong H M, Jeon J U and Kim Y K 2003 Silicon micro *XY*-stage with a large area shuttle and no-etching holes for SPM-based data storage *J. Microelelctromech. Syst.* **12** 470–8

[13] Lu M S-C and Fedder G K 2004 Position control of parallel-plate microactuators for probe-based data storage *J. Microelectromech. Syst.* **13** 759–69

[14] Liu X, Kim K and Sun Y 2007 A MEMS stage for 3-axis nanopositioning *J. Micromech. Microeng.* **17** 1796–802

[15] Mukhopadhyay D J, Dong J, Pengwang E and Ferreira P M 2008 A SOI MEMS based 3-DOF planar parallel-kinematics nanopositioning stage *Sensors Actuators* A **147** 340–51

[16] Gu Lei, Li Xinxin, Bao Haifei, Liu Bin, Wang Yuelin, Liu Min, Yang Zunxian and Cheng Baoluo 2006 Single-wafer-processed nano-positioning *XY*-stages with trench-sidewall micromachining technology *J. Micromech. Microeng.* **16** 1349–57

[17] Yeom D H, Park N J and Jung S Y 2007 Digital controller of novel voice coil motor actuator for optical image stabilizer *Int. Conf. on Control, Automation and Systems* pp 2201–6

[18] Sato K, Ishizuka S, Nikami A and Sato M 2005 Control techniques for optical image stabilizing system *IEEE Trans. Consum. Electron.* **39** 461–6

[19] Yasuhiro Okamoto and Ryuichi Yoshida 1998 Development of linear actuators using piezoelectric elements *Electron. Commun. Japan 3* **81** 11–7

[20] Chen G-R, Yeh Y-M, Wang S-J and Chiang H-C 2000 A novel structure for digital image stabilizer *IEEE Asia-Pacific Conf. on Circuits and Systems* pp 101–4

[21] Mohamed A, Elsimar H and Ismail M 2003 Analysis, and optimization of a CMOS vertical thermal actuator *Proc. Symp. Design, Test, Integration and Packaging of MEMS/MOEMS* pp 214–7

[22] Sachs D, Nasiri S and Goehl D Image stabilization technology overview http://www.invensense.com/shared/pdf/ImageStabilizationWhitepaper_051606.pdf

[23] Lee C-C, Chen W-C, Lee Sz-Yuan and Fang W 2010 Design and implementation of a novel polymer joint for thermal actuator current and thermal isolation *Proc. IEEE Int. Conf. Micro Electro Mechanical Systems* pp 156–9

[24] Que L, Park J-S and Gianchandani Y B 1999 Bent-beam electro-thermal actuators for high force applications *Proc. IEEE Int. Conf. Micro Electro Mechanical Systems* pp 31–36

[25] Lin C-Y and Chiou J-C 2011 Design, fabrication and actuation of 4-axis thermal actuating image stabilizer *Micro Nano Lett.* **6** 549–52

[26] Chiou J C, C-C Hung and Lin C-Y 2010 Design, fabrication, and actuation of a MEMS-based image stabilizer for photographic cell phone applications *J. Micromech. Microeng.* **20** 075025

[27] Yu A B, Zhang X M, Cai H, Zhang Q X and Liu A Q 2007 Rhombic-shaped thermal actuator array for evenly-distributed very large displacement *IEEE Int. Conf. on Micro Electro Mechanical Systems (Kobe, Japan)* pp 663–6

[28] Randall J E and Stiles R N 1964 Power spectral analysis of finger acceleration tremor *J. Appl. Physiol.* **19** 357–60

[29] Barkley G B 2000 Using an accelerometer sensor to measure human hand motion Massachusetts Institute of Technology, USA

[30] Chiu C-W, Chao Paul C-P and Wu D-Y 2007 Optimal design of magnetically actuated optical image stabilizer mechanism for cameras in mobile phones via genetic algorithm *IEEE Trans. Magn.* **43** 2582–4

[31] Lee J-C and Lee D-W 2009 Fabrication of a micro *XY*-stage using SU-8 thermal actuators *Microelectron. Eng.* **86** 1267–70

[32] Lau G K, Duc T C, Goosen J F L, Sarro P M and van Keulent F 2007 Power efficient v-shape electro-thermal

actuator using constrained Su-8 *Transducer and Eurosensors (Lyon, France)* pp 287–90

[33] Henneken V A, Sassen W P, van der Vlist W and Wien W H A 2008 Two-dimensional fiber positioning and clamping device for product-internal microassembly *J. Microelectromech. Syst.* **17** 724–34

[34] Messenger R K, McLain T W and Howell L L 2006 Piezoresistive feedback for improving transient response of MEMS thermal actuators *Proc. SPIE* **6174** 617408

[35] Maloney1 M J, Schreiber D S and DeVoe Don L 2004 Large-force electrothermal linear micromotors *J. Micromech. Microeng.* **14** 226–34

[36] Geisberger A, Kadylak D and Ellis M 2006 A silicon electrothermal rotational micro motor measuring one cubic millimeter *J. Micromech. Microeng.* **16** 1943–50

[37] Song M-G, Hur Y-J, Park N-C, Park Y-P and Park K-S 2009 Development of small sized actuator for optical image stabilization *ISOT 2009: Int. Symp. on Optomechatronic Technologies* pp 152–7